Research Article | Vol. 28, No. 25 / 7 December 2020 / Optics Express 37788
Optics EXPRESS

Laser wavelength metrology with low-finesse etalons and Bayer filters

J. Nicholas Porter,[1,*] Jarom S. Jackson,[1,2] Dallin S. Durfee,[1,3] and Richard L. Sandberg[1]

[1]Department of Physics and Astronomy, Brigham Young University, N261 Eyring Science Center, Provo, Utah 84602, USA
[2]NSWC Panama City Division, Naval Surface Warfare Center, Panama City, FL 32407, USA
[3]Department of Physics, Utah Valley University, MS179 800 W. University Parkway, Orem, Utah 84058, USA
[*]j.nicholas.porter@gmail.com

Abstract: We present a wavelength meter with picometer-scale resolution based on etaloning effects of inexpensive glass slides and the built-in color filters of a consumer grade CMOS camera. After calibrating the device to a commercial meter, we tested the device's calibration stability using two tunable visible lasers for a period of over 16 days. The wavelength error over that entire period has a standard deviation of 5.29 parts per million (ppm) about a most probable error of 0.90 ppm. Within 24 hours of calibration, this improves to 0.04 ppm with a standard deviation of 3.94 ppm.

1. Introduction

Single-frequency lasers tuned to a specific wavelength are used in a wide variety of commercial and fundamental research applications [1–9]. In these applications, a wavemeter is typically employed to allow one to tune the laser near to the required wavelength [4]. While many different types of wavemeters exist [10–17], the size, fragility, power requirements, and cost of many wavemeters with picometer accuracy can be limiting in many applications, especially educational use and experiments requiring portability.

Alternative wavemeter designs have been explored [18–23], each with their own advantages and drawbacks. Of particular relevance to the present work are designs based on Fabry-Pérot etalons [17,24–26]. These avoid some of the pitfalls of scanning interferometers; without moving parts, they can be made more compact and robust. High-precision etalon-based wavemeters have generally been associated with high-finesse, near-perfectly flat etalons. This need not be the case.

In 2015, our research group observed etalon interference while working on a wavemeter based on commercial color-sensor chips [27]. These chips measure the intensity of incoming light through red, green, blue, and clear filters. Although they were not designed for it, the reflective surfaces of the color filters were flat enough to create some low-finesse etalon interference. By measuring the spectral responsivity function of each color channel, which included both the color filtering and the etaloning, this work resulted in sub-angstrom wavelength resolution in a device that was compact, less expensive, and more mechanically robust than commercial devices with similar precision.

In this paper we describe a new device that utilizes a series of imperfectly flat etalons to create a spatially varied, wavelength-dependent interference pattern. This pattern is then sampled at many points with a CMOS image sensor. The etalon interference pattern, combined with the image sensor's built-in color filtering, gives each pixel a unique spectral responsivity. By measuring the response curves of many pixels over a range of known wavelengths, we can then determine an unknown wavelength within the same range with picometer-scale resolution. We

#409466 https://doi.org/10.1364/OE.409466
Journal © 2020 Received 8 Sep 2020; revised 17 Nov 2020; accepted 18 Nov 2020; published 1 Dec 2020

Optics EXPRESS

demonstrate this over two relatively narrow ranges of wavelengths (0.1 nm and 0.16 nm wide) within the visible spectrum.

We call this method "Etaloning Laser Interference Analysis Spectrometry" or ELIAS. Like any technique, ELIAS has some disadvantages. For example, it lacks the ability to extrapolate values beyond the explicitly calibrated range. However, there are also some strong advantages. As in the color sensor design, the primary advantage of the ELIAS device is its simplicity—the device is easy to build using less than $100 of hardware. This makes it a viable design for both mass production and in-lab construction. It is also compact, robust, and doesn't require much power to run. These benefits could be potentially useful for experiments that require portability or environmental exposure, though further testing will be needed to demonstrate these advantages.

2. Design

The device (see Fig. 1) consists of an aluminum enclosure wherein a multi-pixel detector and three etalons are rigidly mounted to an actively temperature-stabilized mount. A single-mode optical fiber is fixed to the opposite end of the enclosure 15 cm from the detector such that light diverging from the end of the fiber passes through the etalons and onto the detector. As monochromatic light passes through the etalons, it creates a wavelength-dependent interference pattern that is measured by the detector.

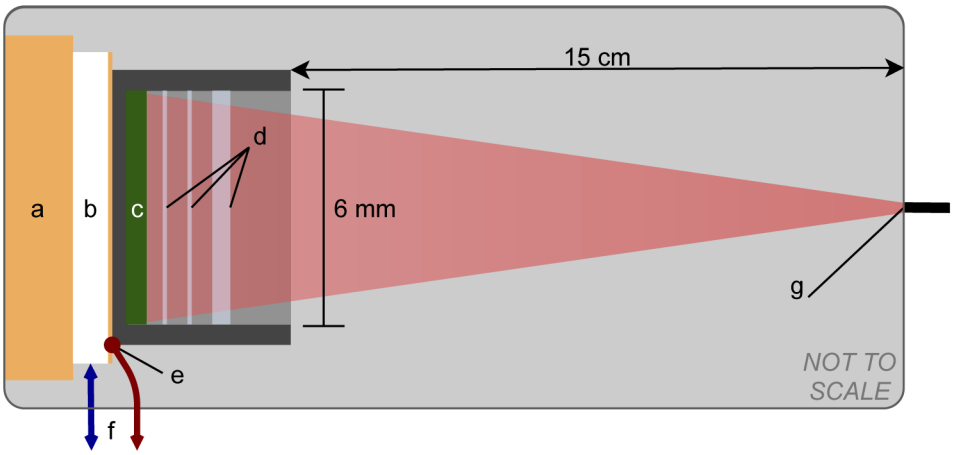

Fig. 1. A simplified schematic of the ELIAS device showing light to be measured diverging out of the optical fiber, passing through the etalons, and being collected on the temperature-controlled webcam. Labelled in this diagram: (a) copper heat sink, (b) thermoelectric cooler (TEC), (c) CMOS image detector, (d) etalons, (e) thermistor, (f) wires connecting to a temperature controller, (g) single-mode optical fiber input.

The detector in our device is a Raspberry Pi Camera Module V.2 containing an 8 megapixel Sony IMX219 CMOS image detector. This choice was, in part, inspired by the recent trend of using webcams as low-cost replacements for scientific image detectors [23,28–30]. The lens is removed from the camera, and the board containing the detector is separated from the rest of the camera module, allowing it to be mounted directly to the temperature controlled mount. The camera is run in "Bayer mode" [29,30], which forgoes all image processing and returns only the raw data collected by the image detector pixels. The device is controlled by a Raspberry Pi 3 Model B+ single-board computer mounted to the outside of the enclosure.

The image sensor has some drawbacks and advantages compared to the color-sensor chip used in our previous work. The image sensor's Bayer filter consists of only three different color filters, unlike the color-senor chip which has a "clear" channel in addition to the red, blue, and

Optics EXPRESS

green filters. Additionally, the image sensor has a dynamic range of 10 bits, compared to the 16-bit outputs of the color sensor. From prior calculations and simulations we expected 10 bits to be sufficient for picometer-level resolution (though a detector with a higher dynamic range and/or quantum efficiency would likely improve the wavemeter's resolution). The advantages of the image sensor are the larger number of pixels and the ability to address each of the pixels independently. By measuring many points in many slightly different etalon interference patterns, and by being able to measure each point independently, such that the pattern is not blurred by averaging over separated detectors as is the case in the color sensor chip, we hoped to acquire more information and achieve higher wavelength resolution and better wavelength discrimination.

To produce high-visibility fringes, etalons in a Fabry-Pérot interferometer must have a thickness which is constant to within a fraction of the light's wavelength over the area in which light is detected [13,17,24–26,31]. In the ELIAS device, etalon flatness requirements are greatly reduced by the proximity of the etalons to the image detector and the small 1.12 μm × 1.12 μm area of each pixel. Even non-precision optics are sufficiently flat over such a small distance.

The etalons in the ELIAS device are two 0.1 mm thick microscope slide covers and one 0.5 mm thick microscope slide. For light with a wavelength of 500 nm, and assuming an index of refraction of 1.5, these have an expected free spectral range (FSR) of 0.833 nm and 0.167 nm respectively. The use of multiple etalons [17,24–26] can increase the density of peaks in the spectral response without losing the fine features of the fringes themselves [32,33]. The low reflectivity of the bare glass surfaces results in a very low finesse. Aside from the obvious disadvantages of low-finesse etalons, there are two significant advantages. First, with a high-finesse etalon it is very unlikely that any particular wavelength will be at a point where the spectral response has a significant slope. But with low-finesse etalons, obtaining useful wavelength information is highly probable with a measurement of a small number of pixels, without the need to scan the etalon thickness or the wavelength of the laser. Second, using uncoated, standard microscope slides and slide covers makes the device simple and inexpensive to fabricate.

Another advantage of using standard microscope slides is that, as the glass is not optically flat, thickness variations over the area of many pixels result in a slightly different FSR—and therefore a different spectral response curve—for each pixel. This increases the information acquired when measurements are made on many different pixels. However, if we think of the etalon interference pattern as a two-dimensional function across the pixels, once data has been collected at a large number of points over the scale of the features in this pattern, we would not expect significant increases in the accuracy. Furthermore, increasing the pixel count will not overcome systematic effects such as temperature drift. We might expect an uncertainty model to look like

$$\sigma(N) = \frac{a}{\sqrt{N}} + b, \tag{1}$$

where σ is the uncertainty, N is the number of pixels, and a and b are constants determined by a number of factors. The constant a would be affected primarily by the quality of each pixel as a detector, while the constant b would be largely dependent on the effective FSR of the multi-etalon system , the spatial variation in the FSR across the pixels, and the dynamic range or bit depth of each pixel. To a certain extent uncertainty would improve with the inclusion of more pixels, but would be fundamentally limited by the complexity of the interference pattern and the precision with which each pixel could measure the pattern at each location. Because of the time required to do calibration fits on each pixel and then to use these fits to calculate an unknown wavelength, in this work we used only $N = 1000$ randomly selected pixels of the 8.08 million pixels on the image sensor. As discussed later, this turned out to be sufficient to reach the point at which additional pixels do not significantly improve wavelength uncertainty.

The temperature of the image sensor and the etalons is controlled using a thermoelectric cooler (TEC) mounted to a copper heat sink and a thermistor placed against the side of the camera

Optics EXPRESS

module. For the duration of the testing period (see Section 4), the temperature controller held the thermistor (and presumably the camera and etalons) at a constant temperature to within a few hundredths of a degree Celsius. The most thermally expansive part of the detector block is the plastic housing around the camera, with an approximate thermal expansion coefficient of $\alpha = 5 \times 10^{-5}$ K^{-1}. This corresponds to a maximum thermal expansion on the order of nanometers—well below the wavelength of our lasers. We had a commercial temperature controller available, and used that in our experiments. Because temperature controllers can be made simply and inexpensively in-lab, the cost of the commercial temperature controller was not included in our cost estimate of the ELIAS device.

3. Calibration and use

To make a measurement at a given wavelength, five images are taken by the image detector. The images are then averaged, resulting in a value Y_p for each pixel p. This process takes a few seconds. To reduce sensitivity to the overall intensity, the value at each pixel is normalized to the average of all of the pixels to produce the normalized pixel values y_p:

$$y_p = \frac{Y_p}{\frac{1}{N}\sum_{i=1}^{N} Y_i}. \tag{2}$$

The normalized pixel values of the previously selected 1000 pixels are then compared to their respective spectral response functions to determine the unknown wavelength of the laser light.

To calibrate the device, measurements are made over a range of known wavelengths. Then for each pixel p the spectral response function $f_p(\lambda)$ is determined by doing a least-squares polynomial curve fit as a function of wavelength to the different values of y_p measured at the different known wavelengths. This polynomial represents the normalized pixel value we would ideally expect to measure on pixel p if the device was measuring a laser with a wavelength of λ. Figure 2 illustrates calibration data and polynomial fits for four arbitrary pixels over the tuning range of the laser used for this particular test.

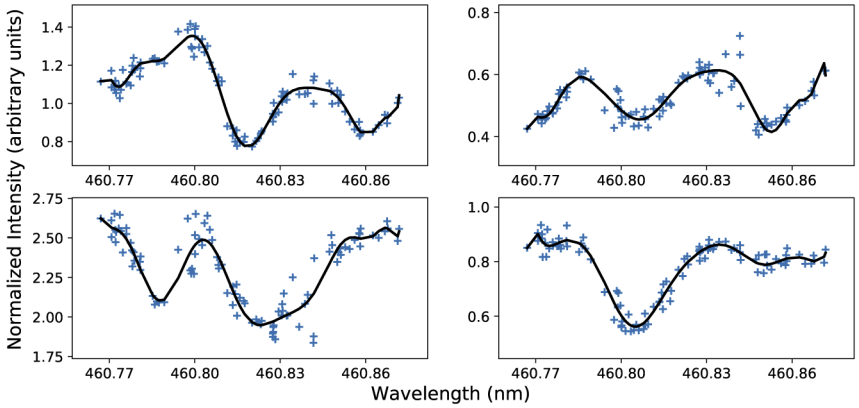

Fig. 2. Calibration data and derived polynomial fits for four selected pixels. The normalized pixel values are shown as plus signs, and the polynomial fits are shown as solid lines.

Care must be taken when selecting the polynomial order for the spectral response curve fits of each pixel. If it is too low, the fit will not follow the fine features of the spectral response. If the order is too high, non-physical fitting to noise will occur. As such, fitting for each pixel is done in an iterative process, incrementing the polynomial order until the fit residual either stops improving or falls below 0.4% of the average response value, up to a maximum order of 15. This process was found to result in a useful calibration for most if not all selected pixels.

Optics EXPRESS

Once the device is calibrated, an unknown wavelength can be measured by comparing the normalized pixel values y_p measured for the unknown wavelength to the calibration spectral response curve fits $f_p(\lambda)$. To do this we calculate a cost function for each pixel,

$$C_p(\lambda) = \left(f_p(\lambda) - y_p\right)^2. \tag{3}$$

We expect the measured value y_p to be close to the response curve of the pixel $f_p(\lambda)$ evaluated at the correct wavelength, such that cost function for the pixel should be small at the wavelength being measured. Because the transmission of an etalon is oscillatory, we expect the cost function for any given pixel to have multiple local minima for any measurement. However, because the spectral response of each pixel is different, the minima in the cost function should be at different wavelengths for different pixels, such that the only wavelengths for which the cost function is small for all pixels would be near the true wavelength being measured. To determine that wavelength, we minimize the function

$$C_{\text{total}}(\lambda) = \sum_{p=1}^{N} (f_p(\lambda) - y_p)^2, \tag{4}$$

which is the sum of the cost functions over all of the pixels. Note that the unknown (measured) wavelength must be within the range of wavelengths over which the device was calibrated.

As with most laser wavelength meters designed for use with single-frequency lasers, our calibration and measurement methods assume that the laser linewidth is much narrower than any features in the spectral response curves. Given the low finesses of the etalons in this device, this assumption should be valid for almost any single-frequency continuous wave laser. If this is not the case, the spectral response curves will depend on both the linewidth and the lineshape of the laser, making it much more difficult or even impossible to determine a central wavelength with this device.

4. Testing

We tested the ELIAS device over a period of 400 consecutive hours with two external-cavity diode lasers (ECDLs) — a blue laser centered at 460.82 nm (with a tuning range of 460.77–460.87 nm) and a red laser centered at 657.45 nm (with a tuning range of 657.36–657.53 nm). An automated shutter system was used to make separate measurements of the two lasers. Data was taken approximately every 80 seconds, for a total of more than 18,000 measurements per laser. The experiment was run from the ELIAS device's Raspberry Pi using Python scripts. The software developed to run the experiment and analyze the data is available online (see Ref. [34]).

Before collecting data, the experiment went through a setup phase in which the script randomly selected the pixels to be measured, determined optimum camera parameters (such as exposure and gain) and fixed them so that they would be the same for every measurement, and ran several quick diagnostic tests. Upon a successful execution of the setup phase, the script began taking data alternately from the two lasers. For calibration and comparison, the wavelength of the laser beam being measured was simultaneously measured by a Bristol 521 commercial wavelength meter. Because the collection time for the Bristol 521 is very fast, 100 wavelength measurements were averaged for each ELIAS measurement.

After each measurement both lasers were set to a new random wavelength, and the experiment paused for 60 seconds before taking another measurement. To prevent the camera from cooling during this pause, the script constantly took pictures and discarded the data until the next measurement began. Only the raw image data was collected during each test, with calculations being done afterward.

Optics EXPRESS

5. Results and discussion

The data for the two lasers was analyzed separately. For each laser, the first 100 ELIAS measurements, along with the corresponding measurements from the Bristol 521, were used to generate the calibration polynomials fits. The rest of the data was analyzed using the calibration to compute the wavelength for each measurement. We then calculated the error for each measurement by taking the difference between the computed wavelength and the wavelength measured by the Bristol 521 commercial reference. In order to compare both lasers' data, we give these values in wavelength parts per million (ppm), not to be confused with picometers (pm). One part per million is 0.657 pm for the red laser, and 0.46 pm for the blue laser.

Histograms of the measurement errors are shown in Fig. 3. The average measurement error (combined for both lasers) is +0.90 ppm, with a standard deviation of ±5.29 ppm. Analyzing the data in 24-hour segments (analogous to recalibrating the device every 24 hours) reduces the average error to +0.04 ppm with a standard deviation of ±3.94 ppm.

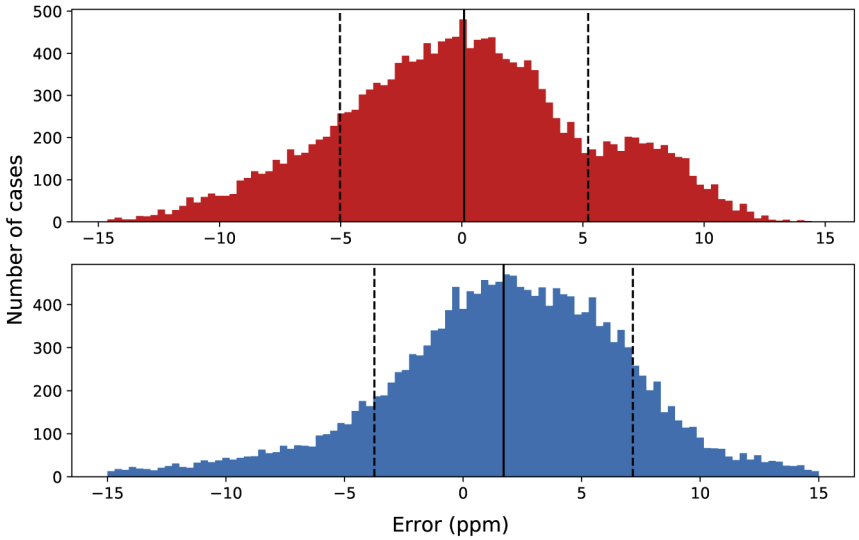

Fig. 3. Measurement error distribution histograms showing the number of independent measurements and their difference from the Bristol 521 measurement. The top histogram reflects measurements taken with the 657 nm laser, while the bottom histogram reflects those taken with the 460 nm laser. The solid vertical line indicates the mean error in each figure; dashed vertical lines indicate one standard deviation from the mean. Outliers have been excluded in this figure.

The Bristol 521 which we used as our reference has a specified accuracy of ±10 ppm [35]. It has a specified repeatability of ±2 ppm over a time scale of 5 minutes, and in previous experiments using a laser locked to an atomic reference [27] we measured the commercial reference to have a stability on the order of 2 ppm over hundreds of hours. As such, while it is likely that a non-negligible amount of the error we measured is due to drift in our commercial reference, possibly even dominating on short time scales, the error in Fig. 3 is probably a good representation the ELIAS device's long term drift.

Although the experimental method was nearly identical for both lasers, there were significant differences in the measurement errors associated with each one. As can be seen in Fig. 4, measurements of the blue laser had more short-term scatter, while the red laser measurements exhibit a larger long-term drift over the 400-hour test period. Fig. 5 shows a very clear correlation of measurement error with wavelength for the blue laser (which could potentially be calibrated

Optics EXPRESS

out). This was much less visible in the red laser, possibly because it was smeared out and masked by the greater long term drift.

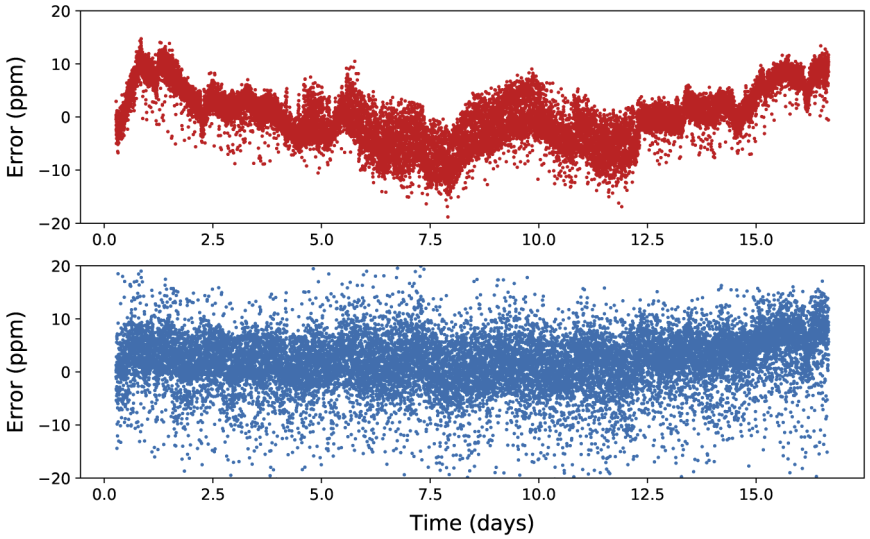

Fig. 4. Measurement error with respect to time. Error in measurements taken with the 657 nm laser are shown in red (top), and data taken with the 460 nm laser are shown in blue (bottom).

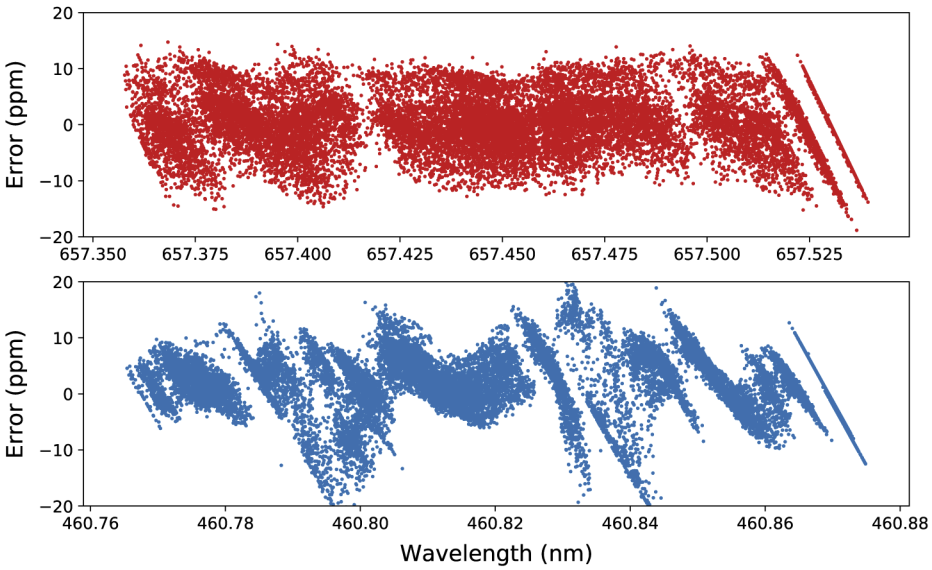

Fig. 5. Measurement error with respect to wavelength over the 400 hr period. Error in measurements of the 657 nm laser are shown in red (top), and error in measurements of the 460 nm laser are shown in blue (bottom).

The Allan deviation for measurements of both lasers is shown in Fig. 6. Because the lasers were randomly tuned for each measurement, the wavelength dependence in the blue laser's error causes its Allan deviation to be large for small values of τ. The long-term drift in the red laser's measurement error causes its Allan deviation to be large for large values of τ.

Optics EXPRESS

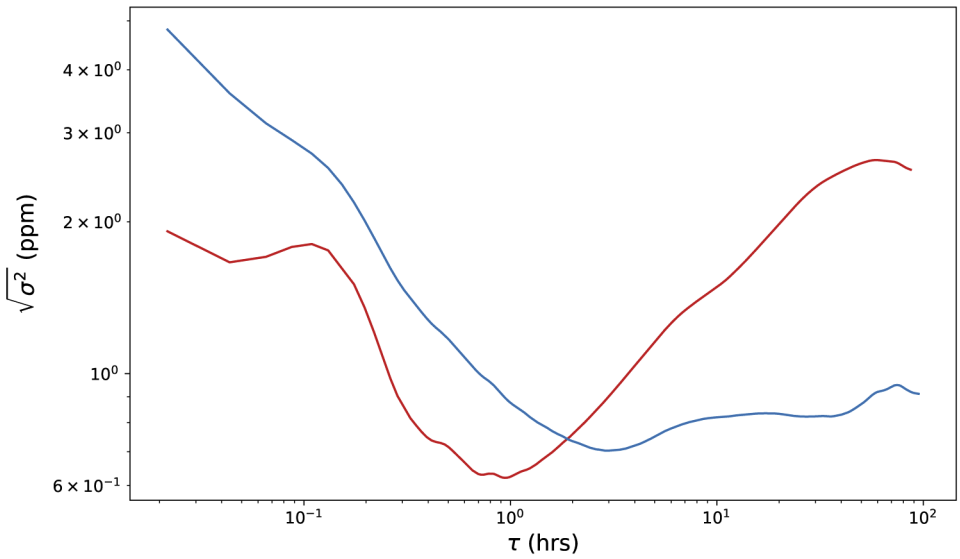

Fig. 6. Allan deviation of measurement error. For short timescales (τ<2 hr), the Allan deviation error was smaller in the 657 nm laser measurements (red). For long timescales (τ>2 hr), it was smaller in the 460 nm laser measurements (blue).

We currently believe that the larger long-term drift in the red laser measurements were due to the fact that in each measurement the red laser wavelength was measured first after the 60-second pause between measurements. Even though steps were taken to prevent it, the camera may have briefly heated up at the beginning of each measurement, causing a small temperature transient.

The number of pixels used in the cost function (see Eq. (4)) also has a significant effect on the calculated wavelength's error. Figure 7 shows the standard deviation wavelength error when

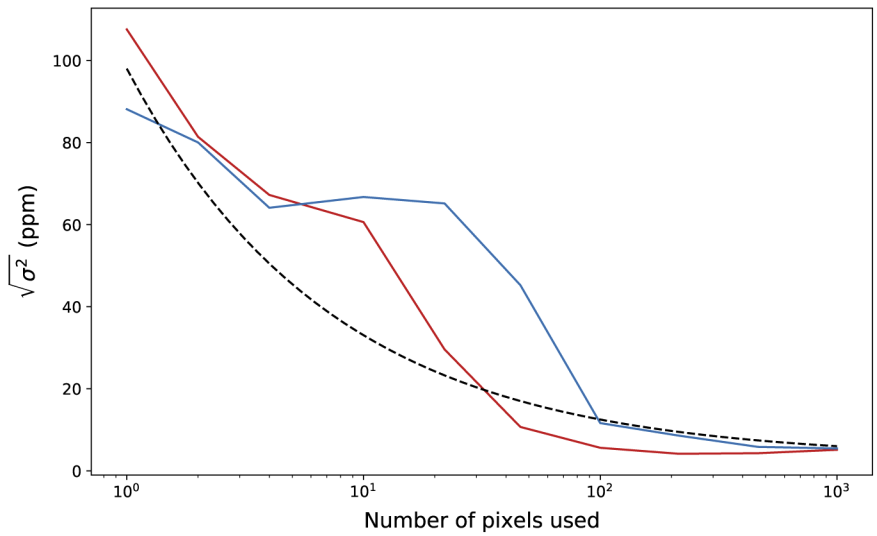

Fig. 7. Standard deviation measurement error with respect to the number of pixels used in wavelength calculation. Uncertainty roughly follows the model given in Eq. (1) (dashed) in both the 657 nm laser measurements (red) and the 460 nm laser measurements (blue).

Optics EXPRESS

various random subsets of the full 1000 pixels are used, along with the hypothesized uncertainty model given in Eq. (1). While uncertainty clearly improves with the number of pixels, it appears to level off before 1000 pixels. This suggests that, without additional etalons to further complicate the interference patterns, little would be gained from the use of more pixels.

6. Future work

It is possible that improved thermal stability, or wavelength corrections based on measured temperatures, could improve the performance of our device. Also, while the combination of color filters and etalon effects should allow the device to be used over a broad range of wavelengths, the calibration method we currently use, involving curve fits to pixel spectral response functions, does not naturally extend itself to allow a single calibration to cover the entire visible spectrum. A more fundamental understanding of the spectral response curves and/or a machine learning scheme could possibly be used for broadband calibration.

7. Conclusion

We have designed and constructed a simple-to-build wavelength meter with picometer-level resolution using less than $100 of materials. We have tested the device using a commercial wavelength meter as a reference over a continuous period of 400 hours. The simplicity, low cost, mechanical robustness, and low power requirements could make this device useful in a wide range of applications.

Funding

Brigham Young University; College of Science at Utah Valley University.

Acknowledgments

We would like to acknowledge Nils Otterstrom, Tyler Jones, and James Archibald for their work on the color sensor wavemeter which led directly to this work. We would also like to thank Jonathan Treter, Dallen Petersen, Ben Whetton, and Carter Day, who offered support and advice in our shared lab space.

Disclosures

The authors declare no conflicts of interest.

References

1. B. Welz and M. Sperling, *Atomic absorption spectrometry* (John Wiley & Sons, 2008), chap. 23.
2. V. M. Baev, T. Latz, and P. E. Toschek, "Laser intracavity absorption spectroscopy," Appl. Phys. B **69**(3), 171–202 (1999).
3. M. Lackner, "Tunable diode laser absorption spectroscopy (TDLAS) in the process industries–a review," Rev. Chem. Eng. **23**(2), 65 (2007).
4. L. Couturier, I. Nosske, F. Hu, C. Tan, C. Qiao, Y. Jiang, P. Chen, and M. Weidemüller, "Laser frequency stabilization using a commercial wavelength meter," Rev. Sci. Instrum. **89**(4), 043103 (2018).
5. W. D. Phillips, "Nobel lecture: Laser cooling and trapping of neutral atoms," Rev. Mod. Phys. **70**(3), 721–741 (1998).
6. D. J. Wineland and W. M. Itano, "Laser cooling of atoms," Phys. Rev. A **20**(4), 1521–1540 (1979).
7. Z. Xu, W. Zhuang, Y. Wang, D. Wang, X. Zhang, X. Xue, D. Pan, and J. Chen, "Lasing of cesium four-level active optical clock," in *2013 Joint European Frequency and Time Forum & International Frequency Control Symposium (EFTF/IFC)*, (IEEE, 2013), pp. 395–398.
8. W. Oskay, S. A. Diddams, E. A. Donley, T. M. Fortier, T. P. Heavner, L. Hollberg, W. M. Itano, S. R. Jefferts, M. Delaney, K. Kim, F. Levi, T. E. Parker, and J. C. Bergquist, "Single-atom optical clock with high accuracy," Phys. Rev. Lett. **97**(2), 020801 (2006).
9. M. Schioppo, R. C. Brown, W. F. McGrew, N. Hinkley, R. J. Fasano, K. Beloy, T. H. Yoon, G. Milani, D. Nicolodi, J. A. Sherman, N. B. Phillips, C. W. Oates, and A. D. Ludlow, "Ultrastable optical clock with two cold-atom ensembles," Nat. Photonics **11**(1), 48–52 (2017).

Optics EXPRESS

10. R. Castell, W. Demtröder, A. Fischer, R. Kullmer, H. Weickenmeier, and K. Wickert, "The accuracy of laser wavelength meters," Appl. Phys. B **38**(1), 1–10 (1985).
11. K. Saleh, J. Millo, A. Didier, Y. Kersalé, and C. Lacroûte, "Frequency stability of a wavelength meter and applications to laser frequency stabilization," Appl. Opt. **54**(32), 9446–9449 (2015).
12. J. Ishikawa, N. Ito, and K. Tanaka, "Accurate wavelength meter for cw lasers," Appl. Opt. **25**(5), 639–643 (1986).
13. R. F. Nabiev, C. J. Chang-Hasnain, L. E. Eng, and K.-Y. Lau, "Monolithic wavelength meter and photodetector using a wavelength dependent reflector," (1996). US Patent 5760419A.
14. M. Muneeb, A. Ruocco, A. Malik, S. Pathak, E. Ryckeboer, D. Sanchez, L. Cerutti, J. Rodriguez, E. Tournié, W. Bogaerts, M. K. Smit, and G. Roelkens, "Silicon-on-insulator shortwave infrared wavelength meter with integrated photodiodes for on-chip laser monitoring," Opt. Express **22**(22), 27300–27308 (2014).
15. P. Fox, R. Scholten, M. Walkiewicz, and R. Drullinger, "A reliable, compact, and low-cost Michelson wavemeter for laser wavelength measurement," Am. J. Phys. **67**(7), 624–630 (1999).
16. B. Redding, S. M. Popoff, and H. Cao, "All-fiber spectrometer based on speckle pattern reconstruction," Opt. Express **21**(5), 6584–6600 (2013).
17. N. Konishi, T. Suzuki, Y. Taira, H. Kato, and T. Kasuya, "High precision wavelength meter with Fabry-Perot optics," Appl. Phys. **25**(3), 311–316 (1981).
18. S. Roy, S. Chaudhuri, and C. Unnikrishnan, "A simple and inexpensive electronic wavelength-meter using a dual-output photodiode," Am. J. Phys. **73**(6), 571–573 (2005).
19. M. Mazilu, T. Vettenburg, A. D. Falco, and K. Dholakia, "Random super-prism wavelength meter," Opt. Lett. **39**(1), 96–99 (2014).
20. L. Yan, B. Chen, W. Yang, R. Wei, and S. Zhao, "A novel laser wavelength meter based on the measurement of synthetic wavelength," Rev. Sci. Instrum. **81**(11), 115104 (2010).
21. M. Wakim, S. Topcu, L. Chassagne, J. Nasser, Y. Alayli, and P. Juncar, "Highly accurate laser wavelength meter based on Doppler effect," Opt. Commun. **262**(1), 97–102 (2006).
22. D. F. Gray, K. A. Smith, and F. B. Dunning, "Simple compact Fizeau wavemeter," Appl. Opt. **25**(8), 1339–1343 (1986).
23. J. D. White and R. E. Scholten, "Compact diffraction grating laser wavemeter with sub-picometer accuracy and picowatt sensitivity using a webcam imaging sensor," Rev. Sci. Instrum. **83**(11), 113104 (2012).
24. R. L. Byer and J. A. Paul, "Optical wavelength meter," (1979). US Patent 4,172,663.
25. A. Fischer, R. Kullmer, and W. Demtröder, "Computer controlled Fabry-Perot wavemeter," Opt. Commun. **39**(5), 277–282 (1981).
26. D. Rees and M. Wells, "A precision wavelength meter for a pulsed laser," J. Phys. E: Sci. Instrum. **19**(4), 301–308 (1986).
27. T. B. Jones, N. Otterstrom, J. Jackson, J. Archibald, and D. S. Durfee, "Laser wavelength metrology with color sensor chips," Opt. Express **23**(25), 32471–32480 (2015).
28. F. Cignoli, S. D. Iuliis, and G. Zizak, "A webcam as a light probe beam profiler," Appl. Spectrosc. **58**(11), 1372–1375 (2004).
29. G. Langer, A. Hochreiner, P. Burgholzer, and T. Berer, "A webcam in Bayer-mode as a light beam profiler for the near infra-red," Opt. Lasers Eng. **51**(5), 571–575 (2013).
30. L. M. Richards, S. S. Kazmi, J. L. Davis, K. E. Olin, and A. K. Dunn, "Low-cost laser speckle contrast imaging of blood flow using a webcam," Biomed. Opt. Express **4**(10), 2269–2283 (2013).
31. T. Scholl, S. J. Rehse, R. Holt, and S. Rosner, "Broadband precision wavelength meter based on a stepping Fabry–Pérot interferometer," Rev. Sci. Instrum. **75**(10), 3318–3326 (2004).
32. W. R. Skinner, P. B. Hays, and V. J. Abreu, "Optimization of a triple etalon interferometer," Appl. Opt. **26**(14), 2817–2827 (1987).
33. G. A. Gary, K. Balasubramaniam, and M. Sigwarth, "Multiple-etalon systems for the Advanced Technology Solar Telescope," in *Innovative Telescopes and Instrumentation for Solar Astrophysics*, vol. 4853 (International Society for Optics and Photonics, 2003), pp. 252–272.
34. J. N. Porter, "ELIAS software," https://doi.org/10.5281/zenodo.4008685 (2020).
35. "521-VIS - Bristol Instruments | Optical wavelength meter spec sheet," https://testdyne.com/Datasheets/BristolInstruments_521-VIS_DS.pdf. Accessed August 5, 2020.